Carbon 132 (2018) 370–379

Contents lists available at ScienceDirect

Carbon

journal homepage: www.elsevier.com/locate/carbon

CO_2 oxidation of carbon nanotubes for lithium-sulfur batteries with improved electrochemical performance

Datao Wang [a], Ke Wang [b], Hengcai Wu [a], Yufeng Luo [a], Li Sun [b], Yuxing Zhao [a], Jing Wang [a], Lujie Jia [a], Kaili Jiang [a, c], Qunqing Li [a, c], Shoushan Fan [a], Jiaping Wang [a, c, *]

[a] Department of Physics and Tsinghua-Foxconn Nanotechnology Research Center, Tsinghua University, Beijing 100084, China
[b] School of Materials Science and Technology, China University of Geosciences, Beijing 100083, China
[c] Collaborative Innovation Center of Quantum Matter, Beijing 100084, China

ARTICLE INFO

Article history:
Received 26 December 2017
Received in revised form
2 February 2018
Accepted 11 February 2018
Available online 12 February 2018

Keywords:
Carbon dioxide
Carbon nanotube
Lithium–sulfur battery
Dispersion
Negative charges

ABSTRACT

The fabrication of high-performance cathodes with high sulfur content is essential for the practical realization of lithium–sulfur (Li–S) systems. The preparation of high-sulfur-content electrodes is currently hindered by poor dispersion of the conductive agents; nonuniformly distributed conductive agents cannot provide sufficient sulfur-loading sites, thereby resulting in aggregation of sulfur/Li_2S and severe polarization. To deal with this issue, we prepare CO_2 modified carbon nanotube (CNT)-based cathodes for Li–S batteries. CNTs are exposed to CO_2 at 900 °C, resulting in uniformly distributed negative charges on the external surface of the tubes; the electrostatic repulsion facilitated the dispersion of CNTs. Compared with the previous work on CNTs prepared by air oxidation (denoted as air-CNTs), the dispersions of the CO_2-treated CNTs (denoted as CO_2-CNTs) are more stable, which allows higher sulfur loading and improves sulfur utilization. A free-standing CO_2-CNT&S electrode with a sulfur content of 80 wt% is fabricated through a sonication-assisted method. The excellent dispersion of the CO_2-CNT&S network results in little kinetic barriers, low polarization, and fast charge transport at the interface of the electrode and electrolyte. The CO_2-CNT&S electrode delivers a lower capacity fading rate and superior rate performance compared with the air-CNT&S electrode.

1. Introduction

The consumption of fossil fuels and the resulting environmental issues have led to the search for alternative, sustainable, and clean energy technologies. Rechargeable energy storage devices with high energy density must be developed to fulfill the demands of electric vehicles and portable electronic devices. Among the various energy storage devices, lithium–sulfur batteries (Li–S batteries) have attracted much attention owing to their high theoretical specific capacity (1672 mA h g^{-1}) and energy density (2570 W h kg^{-1}). In addition, sulfur is naturally abundant, nontoxic, and safe [1]. Therefore, the Li–S battery is considered as a promising candidate to achieve a high capacity and low-cost system. However, the practical application of Li–S batteries is hindered by a limited sulfur utilization ratio, low coulombic efficiency, and rapid capacity decay. These challenges arise from the poor electrical conductivity of both sulfur and the discharge product Li_2S, and the dissolution of lithium polysulfides (Li_2S_x, $4 \leq x \leq 8$), which causes intermediates to shuttle between the electrodes [2,3].

To overcome these issues, many research strategies have been devoted to accommodating sulfur and constraining polysulfides by using carbonaceous materials such as mesoporous carbon [1,4], graphene [5–7], carbon nanotubes (CNTs) [8,9], and carbon spheres [10]. Porous carbon hosts also provide pathways for Li^+ ion diffusion and good electronic conductivity, which can improve sulfur utilization and lead to a high capacity [11,12]. However, considering that the conductive carbon skeletons and binder contribute little to the energy storage capacity, the introduction of these inactive components would sacrifice the overall energy density [13]. Therefore, the sulfur loading and battery performance need to be balanced. The reported sulfur content is usually below 75 wt%, and typically approximately 60 wt% [14], which is lower than the weight ratio of the active materials in conventional lithium-ion cells (>90 wt%) [15]. Therefore, enhancing the sulfur loading and

* Corresponding author. Department of Physics and Tsinghua-Foxconn Nanotechnology, Research Center, Tsinghua University, Beijing 100084, China.
E-mail address: jpwang@tsinghua.edu.cn (J. Wang).

https://doi.org/10.1016/j.carbon.2018.02.048
0008-6223/

content is essential for the practical application of Li–S technology. The main challenge for achieving high sulfur content is that a small amount of carbon host is not able to provide sufficient adhesion points for loading of sulfur and trapping intermediate polysulfide, thereby resulting in the aggregation of active materials and poor cycling performance [13]. Advanced architectures with an ultrahigh surface area and sufficient active sites are required to act as an effective carrier for loading a high amount of sulfur [16,17]. Conductive sulfur hosts need to be effectively dispersed without aggregation to fully utilize the available sulfur-loading sites [18].

Owing to the open porous structures, high conductivity, and one-dimensional (1D) flexible nanostructures of CNTs, they are considered as one of the most promising carbon materials as sulfur hosts [19–21]. However, the agglomeration behavior of CNTs decreases the number of sulfur-loading sites, and thereby limits the sulfur loading in CNT&S composite electrodes [19]. To overcome the agglomeration problem, a considerable amount of work has been devoted to functionalizing CNTs to achieve uniform dispersions [22]. Concentrated sulfuric acid has been previously used to exfoliate CNT bundles by oxidizing CNTs [23–25]. Oxidation sites with oxygen-containing groups on the CNTs have been reported for acquiring a negative surface charge, and the electrostatic repulsion owing to the surface charges can facilitate their dispersion [26–30]. However, because the waste produced by the acid-oxidation technology is environmentally unfriendly and corrosive, solvent-free methods need to be developed [22,31–33].

Remarkably, super-aligned CNTs (SACNTs) can partially mitigate the agglomeration problem of CNTs, which can be ascribed to the highly unidirectional alignment [34–36]. In our previous work, we utilized SACNTs to build a highly conductive support skeleton for the formation of a binder-free and current-collector-free electrode for Li–S cells [8,37–39]. Besides the mitigation of agglomeration, SACNTs have demonstrated several other unique advantages in Li–S batteries owing to their high electrical conductivities, large aspect ratio (10^4), excellent mechanical properties, and strong intertube interactions. First, sulfur nanoparticles can directly deposit onto the surface of CNTs, which indicates that each separated CNT has a high sulfur loading capability [8,34,40]. Second, considerable adhesion points on the CNTs were also reported to promote the polysulfide-trapping ability and improve the cycling performance [8]. Moreover, a freestanding CNT network, benefiting from the strong van der Waals forces, can increase the sulfur content and overall energy density of Li–S batteries by the elimination of the binder and aluminum foil current collector, which typically account for 20–40 wt% in the conventional cathode [14,34]. However, the significant intertube interactions can also cause individual nanotubes to combine with neighboring ones, forming CNT bundles, which would result in comparatively low utilization of the active sites for efficient sulfur loading. In fact, a sulfur content of 50 wt% in CNT&S was almost the upper limit while maintaining structural integrity and good electrochemical performance [8,39]. To increase the sulfur content, in our previous work, we used air-CNTs to fabricate CNT-S electrodes for Li–S batteries [39]. The air-CNTs were better-dispersed than pristine CNTs and a higher sulfur content in the electrodes (≤70 wt%) could be achieved with good battery performance.

To better understand the dispersion mechanism of the oxidized-CNTs and further increase the sulfur content, carbon dioxide (CO_2) was used to oxidize SACNTs at 900 °C in this work. In comparison with the air-treatment, CO_2 oxidation introduced oxygen-containing functional groups that were uniformly distributed on the external surfaces of CNTs. The large number of negatively charged functional groups on the CO_2-CNTs produced great electrostatic repulsive forces and achieved a stable dispersion of separated tubes in a mixed ethanol/water solvent. The stable dispersion of CO_2-CNTs allowed an even higher sulfur loading and enhanced sulfur utilization; a CO_2-CNT&S composite electrode with a sulfur content as high as 80 wt% was fabricated. This new type of electrode delivered an initial specific capacity of 736.2 mA h $g^{-1}{}_{sulfur}$ at 0.2 C with a low capacity fading of 0.172% per cycle over 300 cycles and a capacity of 459.6 mA h $g^{-1}{}_{sulfur}$ at a charge rate as high as 5 C, both of which were higher than the performance of the air-CNT&S composite electrode. The well-dispersed CO_2-CNT&S composite and its excellent cell performance confirm that CO_2 oxidation can be a simple but efficient oxidation method for fabricating CNT&S cathodes.

2. Experimental

2.1. Preparation of pristine CNTs, air-CNTs, and CO_2-CNTs

SACNT arrays with a nanotube diameter of 20–30 nm and a height of 300 μm were synthesized on silicon wafers by chemical vapor deposition (CVD), in which iron was used as the catalyst and acetylene as the precursor. Details of the synthesis method can be found in previous papers [36]. Air-CNTs were fabricated by heating SACNTs to 550 °C in air at a rate of 30 °C min^{-1} and maintained at 550 °C for 30 min. CO_2-CNTs were fabricated by heating SACNTs to 900 °C in a CO_2 atmosphere at a rate of 30 °C min^{-1} and maintained at 900 °C for 60 min. The mass loss rates were both below 20% after oxidation.

2.2. Synthesis of CNT&S composites

Both air-CNT&S and CO_2-CNT&S composites were prepared by the following steps. 35 mg of commercial sulfur (Analytical reagent, purity > 99.7%, Beijing Dk Nano Technology Co., Ltd.) was dispersed in 25 mL ethanol by sonication (1000 W) for 15 min and 7.5 mg of CNTs was stirred in 50 mL of a mixed ethanol–water solution (1:4 by volume) simultaneously. The CNTs suspension was added dropwise so that sulfur was uniformly loaded on the nanotubes without self-aggregation. The mixture was sonicated at room temperature for another 30 min to form a homogeneous suspension. After filtration and drying at 40 °C, the CNT&S electrode was obtained. The composites were heated to 155 °C for 12 h in a sealed autoclave. The sulfur content was 80 wt% in the raw materials. The sulfur loading of the composites was 1.4 mg cm^{-2}. The thickness of the electrodes was 70 μm and the dimensions of the electrodes were 0.8 cm× 0.8 cm.

2.3. Characterization

The structure and elemental composition of the electrode were investigated by scanning electron microscopy (SEM; Sirion 200, FEI) and transmission electron microscopy (TEM; Tecnai G2F20, FEI). The wetting behaviors of CNTs were investigated by measuring the contact angles of the water droplets (1 μL) on CNT films. X-ray photoelectron spectroscopy (XPS) analysis was carried out on a PHI Quantera II surface analysis equipment. Thermogravimetric analysis (TGA) of CNTs and air-CNT&S and CO_2-CNT&S composites were performed on a Pyris 1 TGA (PerkinElmer, USA) in air (50–800 °C) and CO_2 (50–1200 °C) in order to determine the weight losses of CNTs, the sulfur contents in the composites, and the contents of functional groups. The Zeta potentials of the CNT dispersions were investigated at a concentration of 0.02 mg mL^{-1} at 25 °C by a Malvern Instrument (Zetasizer Nano ZS90). Raman spectra were conducted on a Horiba spectrometer (633 nm Ar laser, 24 mW). The sheet resistances of the CNT&S films were measured by a four-point method using the ResMap system (Creative Design Engineering Inc., USA). The conductivity (σ) was determined from the thickness

(t) and the sheet resistance (R_S): $\sigma = 1/R_S$ t. Three layers of the pristine and CO_2-treated CNT films were prepared for Fourier transform infrared spectroscopy (FTIR), which was performed on an InGaAs photodetector (Conquer Optical Technology Co.).

2.4. Electrochemical measurements

Coin-type half-cells were assembled in a glovebox filled with protective argon gas (M. Braun Inert Gas Systems Co. Ltd., Germany). The CNT&S composites were directly used as a positive electrode without introducing additional current collectors and binders. Lithium foil was employed as the negative electrode. A polypropylene film (Celgard 2400) was used to separate the cathode and the anode. The electrolyte was 1 M LiTFSI and 0.2 M $LiNO_3$ in DME/DOL with a volume ratio of 1:1. The ratio of electrolyte and sulfur used in the cell was 25 mL g^{-1}. The cycling performances of the cells were tested by a Land battery system (Wuhan Land Electronic Co., China) with cut-off voltages of 1.8–2.6 V. The rate capabilities were studied by using the same instrument. Cyclic voltammetry (CV) and electrochemical impedance spectroscopy (EIS) measurements were performed using a Galvanostat instrument (EG&G Princeton Applied Research 273A). CV scanning rate was 0.1 mv s^{-1}. The frequency range of the EIS measurements was from 10 mHz to 100 kHz with a small perturbation voltage of 5 mV.

3. Results and discussion

3.1. Morphologies and structures of CO_2-CNTs and air-CNTs

The preparation of the CO_2-CNTs and air-CNTs is schematically illustrated in Fig. 1. The CO_2-CNTs were prepared by heating SACNT arrays to 900 °C in a CO_2 atmosphere. Carbon atoms in the CNTs reacted with CO_2 at high temperatures to produce CO, leaving defects on the tube surfaces [41]. Air-CNTs were prepared by heating SACNT arrays to 550 °C in air. Similarly, the carbon atoms reacted with O_2 to produce CO, also leaving defects on the tube surfaces.

The TEM images of pristine CNTs (Fig. 1b), CO_2-CNTs (Fig. 1c), and air-CNTs (Fig. 1d) clearly demonstrate the different morphology changes of the CNTs resulting from oxidation in air and CO_2. The CO_2 oxidation thinned the CNTs and introduced numerous and slight defects uniformly on the tube surface (indicated by the red arrows in Fig. 1c). The outer carbon layers were partially stripped off. No holes or severe deformation were observed on the surface of the CO_2-CNTs. In contrast, the oxidation pattern of the air-CNTs was different from that of the CO_2-CNTs. The defect sites on the air-CNTs typically exhibited a much faster oxidation rate than the well-crystallized sp^2 carbons, and the following steps in the oxidation process were suggested [42,43]: First, oxidation occurred preferentially at the initial structural defects and etch pits were created. During the continuous oxidation process, these etch pits were more easily oxidized than the smooth and stable surface. This process resulted in a high concentration of oxidation sites, which corresponded to the holes at the sidewalls of CNTs (indicated by the red arrows in Fig. 1d). Except for the oxidation sites around the holes, other parts of the CNTs almost remained intact. These TEM results suggest different oxidation patterns in the air-CNTs and CO_2-CNTs: air oxidation prefers to result in isolated and large etching pits along the tube surfaces, while CO_2 oxidation tends to introduce slight defects uniformly at numerous sites on CNTs.

The oxidation treatments reduced the length of CNTs. Since all the CNT arrays before and after oxidation treatments used in this work exhibited a super-aligned structure, the lengths of CNTs can be determined by measuring the heights of the CNT arrays (Fig. S1a). SEM images (Figs. S1c, d, and e) indicated that the average lengths of the pristine CNTs, air-CNTs, and CO_2-CNTs were 312.2±2.0, 287.7±1.2, and 268.1±5.6 μm, demonstrating 8% and 12% decreases in average CNT length by air and CO_2 oxidations respectively.

TGA results of SACNTs in air and CO_2 are shown in Fig. 2a. The main weight losses of the CNTs were observed in the temperature

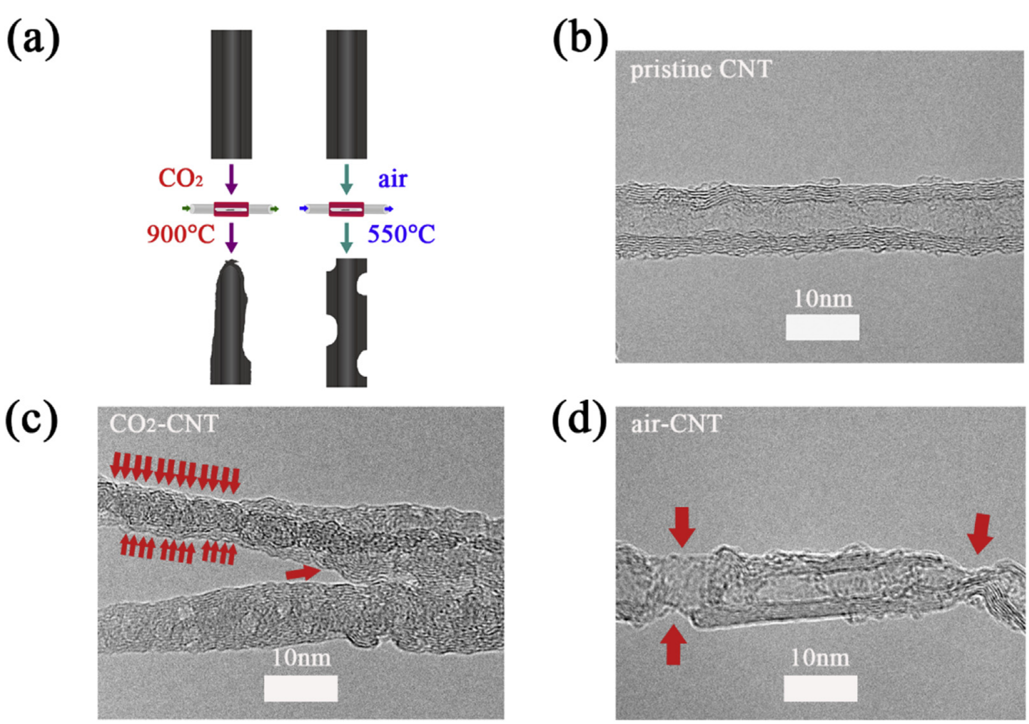

Fig. 1. (a) Schematic diagram of the oxidation procedure for CO_2-CNTs and air-CNTs. High-resolution TEM images of (b) pristine CNT, (c) CO_2-CNT, and (d) air-CNT. The red arrows indicate the oxidation sites. (A colour version of this figure can be viewed online.)

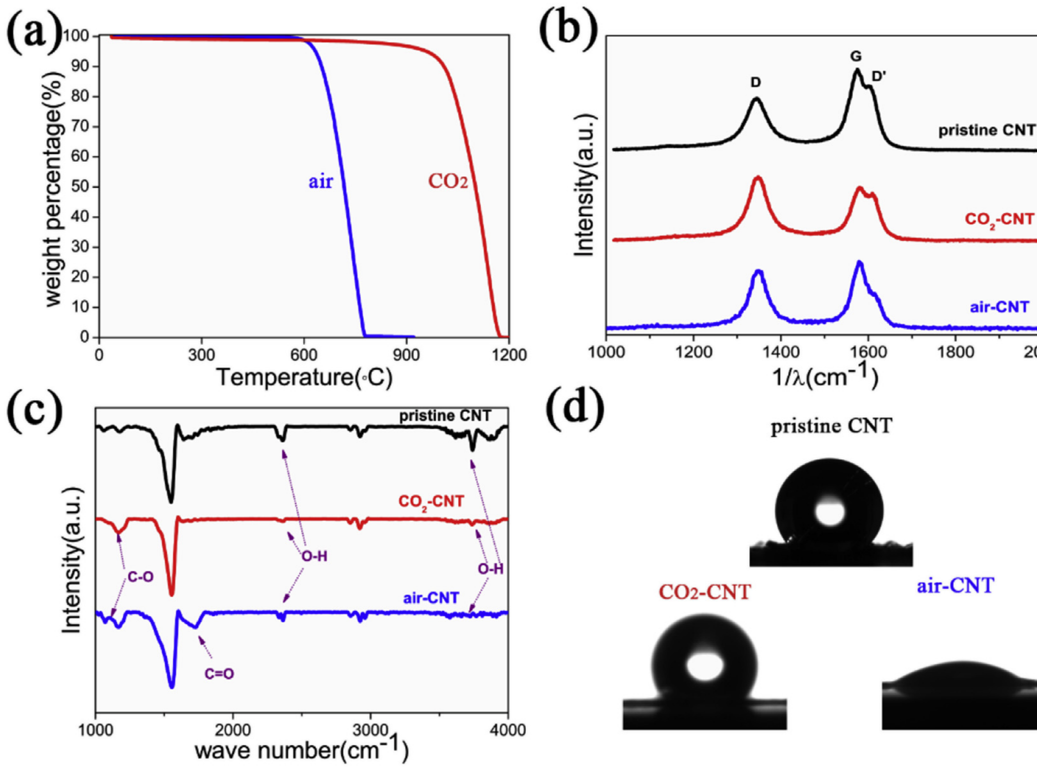

Fig. 2. (a) TGA curves of SACNTs in air and CO_2. (b) Raman spectra, (c) FTIR spectra, and (d) wetting behavior of pristine CNTs, CO_2-CNTs, and air-CNTs. (A colour version of this figure can be viewed online.)

ranges 651–763 °C and 1009–1154 °C, corresponding to the oxidation of the CNTs in air and CO_2, respectively. CNTs could be completely oxidized in both air and CO_2 by further heating at higher temperatures. In order to achieve effective modification of CNTs and meanwhile avoid their severe weight loss, the oxidation treatment parameters were optimized at 550 °C for 30 min in air and 900 °C for 60 min in CO_2, resulting in comparable weight losses (12-18 wt% for the air-CNTs and 13-16 wt% for the CO_2-CNTs).

Raman spectroscopy was carried out to investigate the hybridization changes of the CO_2-CNTs and air-CNTs compared to the pristine CNTs (Fig. 2b). The G band at 1580 cm^{-1} corresponded to the well-crystallized sp^2 carbon atoms. The D band at 1345 cm^{-1} was attributed to the presence of surface defects (sp^3 carbon atoms) [44,45]. Therefore, the defect concentration in the CNTs can be estimated by the I_D/I_G ratio. The pristine SACNTs showed an I_D/I_G ratio of 0.636. After oxidization, the I_D/I_G ratios of the CO_2-CNTs and air-CNTs increased to 1.204 and 0.853, respectively. The above results showed that both air and CO_2 oxidation approaches created defects and changed the hybridization of the carbon atoms from sp^2 to sp^3 and the CO_2-CNTs exhibited the highest sp^3/sp^2 ratio.

Besides changing the hybridization of the carbon atoms, the air and CO_2 oxidation processes also introduced oxygen-containing moieties (C–O/C=O groups) on CNTs. The C1s XPS data for the pristine CNTs, air-CNTs, and CO_2-CNTs are shown in Fig. S2. The peaks at 284.8, 285.5, and 286.5–288.0 eV in the spectra were assigned to sp^2 carbons, sp^3 carbons, and carbons in C–O/C=O bonds, respectively. Compared with the pristine CNTs (Fig. S2a), the increased intensities at 286.5–288.0 eV suggested larger amounts of functional groups with C–O/C=O bonds in both air-CNTs and CO_2-CNTs (Figs. S2b and S2c). The higher binding energies of C1s in the air-CNTs and CO_2-CNTs also suggested that the carbon atoms were partially positive in C–O/C=O bonds and the bonded oxygen atoms at the external tube surfaces had negative charges. The XPS results revealed that both air and CO_2 treatments introduced oxygen-containing functional groups with C–O/C=O bonds on CNTs and enabled the external surfaces of CNTs to be negatively charged, which might be beneficial for their dispersion behaviors.

It is not adequate to evaluate the oxidation patterns in the CO_2-CNTs and air-CNTs only by the ratio of sp^3/sp^2 carbon atoms and the total amounts of functional groups; the spatial distribution of the oxidation sites also needs to be investigated. The perfect sp^2 structure of CNTs typically consists of tertiary carbon atoms. A carbon atom in a C=O bond has 2 bonds to oxygen, and certainly cannot be a tertiary carbon. Therefore, the C=O bonds could only be present at the defect and etching sites of the CO_2-CNTs and air-CNTs where the original hexagonal lattice was destroyed, and thus the intensity of the C=O bonds can indicate the amount of sp^3 carbons at the severely deformed hexagonal lattice. A carbon atom in a C–O bond has a single bond to oxygen and might be a tertiary sp^3 carbon or secondary sp^2 carbon located at etching pits or topological defects. The C–O bonds can be present at any locations of the CO_2-CNTs and air-CNTs. Therefore, the intensity of the C–O bond cannot demonstrate the spatial distribution of the sp^3 carbons [46]. A strategy is proposed in this work that the spatial distribution of the oxidation sites can be estimated by a combination of C=O bond intensity measurements and TEM observations.

Infrared spectroscopy was employed to measure the chemical bond intensities and to assess the structural changes after the oxidization processes (Fig. 2c). For both air-CNTs and CO_2-CNTs, the intensities of the O–H bonds (2361 cm^{-1} and 3728 cm^{-1}) decreased owing to the removal of hydrogen during the oxidation process. The air-CNTs exhibited higher concentrations of both C–O bonds (1160 cm^{-1}) and C=O bonds (1724 cm^{-1}) than the pristine CNTs, indicating the presence of ether, acyl, and carboxyl functional groups in the air-CNTs. Based on the existence of large etch pits in the TEM image (Fig. 1d) and the preferred locations of the C=O bond at severely deformed regions, a large number of acyl and carboxyl functional groups with C=O bonds were probably located at the etch pits where severe deformation occurred in the hexagonal lattice. Because the oxygen atoms in C=O bonds on the external surface of CNTs carried negative charges, the total surface charges were mainly concentrated around the etch pits. The C–O bonds were not restricted to the severe deformation sites on CNTs, and they also contributed to the surface negative charges on the air-CNTs. Compared with the pristine CNTs, the CO_2-CNTs demonstrated a higher concentration of C–O bonds (1160 cm^{-1}) and almost all the C=O bonds (1724 cm^{-1}) disappeared. The initial C=O bonds on the CNTs were preferentially removed by CO_2 as a consequence of their high reactivity [47]. Owing to the absence of O–H and C=O bonds in the CO_2-CNTs, the functional groups on the tube surface were mainly ether moieties with C–O bonds. According to the TEM observations of the homogenous and slight etch pits on the CO_2-CNTs and the widespread distribution of the C–O bonds on tube surfaces, it can be estimated that the oxygen atoms in C–O bonds and the negative charges they carried were uniformly distributed on the external surfaces of the CO_2-CNTs.

The change of the C–O and C=O intensities by the oxidation process affected the wetting behavior of CNTs (Fig. 2d). Both the pristine CNTs and the CO_2-CNTs exhibited large contact angles and similar hydrophobicity, whereas the air-CNTs were hydrophilic and exhibited a much smaller contact angle. The hydrophilicity of the air-CNTs was mainly attributed to the higher C=O and C–O content compared with the pristine CNTs. The hydrophilicity of the CO_2-CNTs remained almost the same compared with the pristine CNTs. The increase in the hydrophilicity of the CO_2-CNTs by an increase in the number of ether functional groups with C–O bonds was offset by the decrease in the number of C=O bonds, because the ether functional groups with C–O bonds are less hydrophilic than the functional groups with C=O bonds owing to the inferior polarity of the C–O bond than that of the C=O bond [48].

Since functional groups containing C-O and C=O bonds have different decomposition temperature ranges in air, the contents of the functional groups can be characterized by TGA [49–53]. TGA curves of the pristine CNTs, air-CNTs, and CO_2-CNTs in air are shown in Fig. S3 and the contents of the functional groups estimated by mass losses at various temperature ranges are summarized in Table S1. Water desorption at temperature lower than 160 °C occurred in all three samples. Compared with the pristine CNTs (0.5 wt% C=O groups and 2.0 wt% C-O groups), the air-CNTs exhibited relatively higher contents of both C=O groups (1.0 wt%) and C–O groups (3.1 wt%). The CO_2-CNTs exhibited the highest contents of C–O groups (5.5 wt%) and the lowest contents of C=O groups (0.2 wt%). These results agree well with the Raman, XPS, FTIR spectra, and wetting behaviors of the air-CNTs and CO_2-CNTs. Although the CO_2-CNTs exhibited a larger total content of functional groups and a higher sp^3/sp^2 ratio than that of the air-CNTs, the contents of functional groups and sp^3/sp^2 ratios might change at various temperatures and heating times in both air-CNTs and CO_2-CNTs.

As discussed earlier, the air-CNTs and CO_2-CNTs demonstrated different modes of distribution of surface negative charges. The surface charges were numerous and uniformly distributed in the CO_2-CNTs, but preferentially located around the etch pits in the air-CNTs. The difference in the surface charge distribution might affect the repulsion potential and their dispersion properties in solution, which were further characterized by Zeta potential measurements and SEM observations. CNT films were obtained by ultrasonication in an ethanol/water solution followed by vacuum filtration and drying. SEM images of the pristine CNT, air-CNT, and CO_2-CNT films are shown in Fig. 3. Apparent bundles and tube aggregation can be seen in the pristine CNTs (Fig. 3a). In the air-CNTs (Fig. 3b) and CO_2-CNTs (Fig. 3c), thinner CNT bundles were evenly distributed, demonstrating their similar dispersity. The densities of the pristine CNT, air-CNT, and CO_2-CNT films were 0.22, 0.25, and 0.26 g cm^{-3}. Even though the air and CO_2 oxidation processes introduced open structure to CNTs, both air-CNT and CO_2-CNT films possessed more condensed structures and higher densities due to their excellent dispersion properties, which are beneficial in achieving high volumetric energy density of CNT&S composite electrode.

Zeta-potential measurements were used to investigate electrostatic interactions and the dispersion stabilities of the pristine CNTs, air-CNTs, and CO_2-CNTs suspensions (Fig. 3d). The pristine CNTs exhibited a zeta potential close to zero (−0.42 mV), whereas the air-CNTs and CO_2-CNTs showed negative values of −6.6 mV and −13.6 mV, respectively (Fig. 3d). These results implied that the pristine CNTs were more likely to aggregate into large bundles because there was almost no negative charge to provide the repulsive force to counterbalance the van der Waals attractive force. The observed negative zeta potentials of the air-CNTs and CO_2-CNTs suggested the presence of negatively charged oxygen atoms in functional groups, and the electrostatic repulsive forces enabled the effective dispersion of CNTs in a ethanol/water solvent, which were consistent with the thinner bundles and less aggregation compared with the pristine CNTs. The CO_2-CNTs exhibited a lower negative zeta potential than the air-CNTs, indicating the superior dispersion stability of the CO_2-CNTs. The stable dispersion of the CO_2-CNTs was mainly attributed to the greater electrostatic repulsive forces provided by the numerous and uniformly distributed negative charges on the tube surface due to the introduction of the oxygen-containing functional groups [54]. For the air-CNTs, negative charges were mainly concentrated at severe defect sites, and a large portion of the tube surfaces still showed the tendency to aggregate owing to the van der Waals force, leading to the dispersion instability of the air-CNTs. The distinct dispersion stability between the air-CNTs and CO_2-CNTs may greatly affect the dispersion properties of the CNTs in composites. In this work, the morphologies and structures of both the CO_2-CNT&S and air-CNT&S composite electrodes were studied.

3.2. *Morphologies and structures of the CNT&S electrodes*

The CNT&S composites were synthesized through a simple ultrasonic-assisted dispersion and vacuum filtration method (Fig. 4a) [8]. The pristine CNT&S electrode with high sulfur content exhibited severe CNT agglomeration owing to the poor dispersity of the pristine CNTs, and it was not possible to fabricate a uniform and flexible high-sulfur-content CNT&S composite electrode. In contrast, the sulfur content of both the air-CNT&S and CO_2-CNT&S electrodes was as high as 80 wt% (determined by TGA, the inset of Fig. 4c and d) owing to the relatively good dispersion, while maintaining a flexible and free-standing electrode structure (Fig. 4b). The sample in Fig. 4b was the CO_2-CNT&S composite, and the air-CNT&S electrode demonstrated similar flexibility. The sulfur loading capabilities of CNT electrodes were highly dependent on the dispersion of the CNTs, especially the number of separated CNTs. Although the air-CNTs exhibited an inferior dispersion stability than the CO_2-CNTs, they still provided sufficient adhesion points to load sulfur particles and to trap the intermediate polysulfides in the air-CNT&S electrodes containing a sulfur content below 70 wt% [39]. However, when the sulfur content was increased to 80 wt%, the air-CNTs had insufficient sulfur-loading sites and the aggregation of sulfur could not be sufficiently inhibited; therefore, the air-CNTs and sulfur particles aggregated into large bundles (Fig. 4c and e). For the CO_2-CNT&S (80 wt%) composites, the majority of the CO_2-CNTs were exfoliated into thin bundles and individual tubes during the ultrasonication process

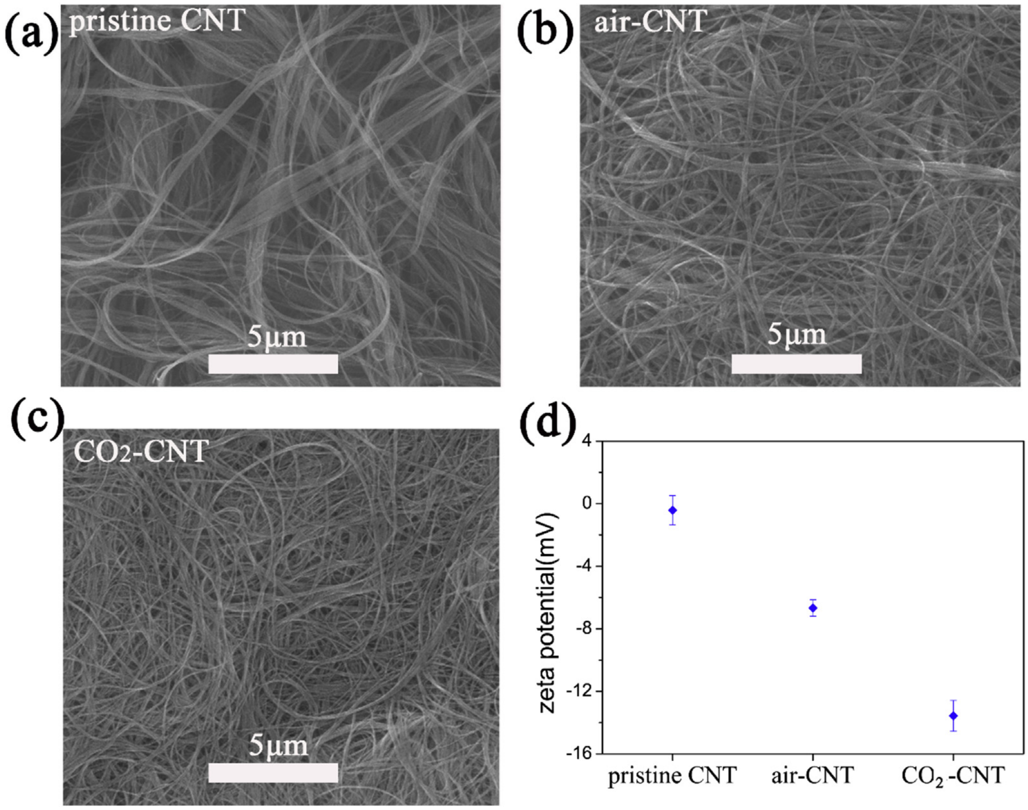

Fig. 3. SEM images of (a) pristine CNTs, (b) air-CNTs and (c) CO_2-CNTs. (d) Zeta potential of the CNTs. (A colour version of this figure can be viewed online.)

due to their superior dispersion stability, and a uniform distribution of both CO_2-CNTs and sulfur were obtained (Fig. 4d and f). Elemental line scanning by EDS (the inset of Fig. 4e and f) implied that a large amount of sulfur layers were uniformly coated on the sidewalls of individual CNTs for both CNT&S composites, which was attributed to the high binding ability of the SACNTs. Note that it was difficult to precisely characterize the morphology and distribution of sulfur by conventional TEM due to the problem of sulfur sublimation in high vacuum [55,56].

Both air-CNT&S and CO_2-CNT&S electrodes demonstrated more condensed structures than the pristine CNT&S electrode. At the same sulfur loading of 60 wt%, the densities of the pristine CNT&S, air-CNT&S, and CO_2-CNT electrodes were 0.164, 0.156, and 0.128 g cm^{-3}, respectively. SEM images of these electrodes are shown in Fig. S4. The pristine CNT&S composite exhibited a poor dispersion with large bundles, the air-CNT&S composite demonstrated an improved dispersion with small bundles, and the CO_2-CNT&S composite showed the best dispersion with the smallest bundles and the most condensed structure due to the superior dispersion stability of the CO_2-CNTs. Even with the open structure of CNTs, the higher density and more condensed structure of the air-CNTs&S and CO_2-CNTs&S electrodes are beneficial in obtaining higher volumetric energy density.

The conductivities of the CO_2-CNT film (8.8 kS m^{-1}) and air-CNT film (9.3 kS m^{-1}) were similar and slightly higher than that of the pristine CNT film (8.4 kS m^{-1}). After introducing insulating S, the conductivity of the CNT&S composites decreased compared with the pure CNT films. The CO_2-CNT&S composite film exhibited a higher conductivity of 2.0 kS m^{-1} than the air-CNT&S film (0.8 kS m^{-1}), owing to the more uniform distribution of the sulfur-coated CO_2-CNTs and the improved electronic contact in the composite [57]. The large number of separated CO_2-CNTs and the higher electrical conductivity of the CO_2-CNT&S composite provided sufficient sulfur-loading sites and promoted sulfur utilization and electron transfer. The well-dispersed CO_2-CNTs&S structure also shortened the lithium-ion diffusion length, acted as 3D continuous electron pathways, permitted good penetration of the electrolyte, and provided sufficient active sites to promote electron and ion transport. The enhanced conductivity and reaction kinetics were expected to result in better cyclic stability and rate capability of the CO_2-CNTs&S electrodes.

3.3. Electrochemical characterization

The cyclic voltammetry (CV) profiles of the air-CNT&S and CO_2-CNTs&S composites are shown in Fig. 5a. For the CO_2-CNTs&S composite, two well-defined reduction peaks were observed at approximately 2.21 V and 1.97 V, corresponding to the reaction from the S_8 ring to Li_2S_x ($4 < x < 8$) and from Li_2S_x ($4 < x < 8$) to Li_2S_x ($1 < x < 4$), respectively [2,3]. In the subsequent charging process, two oxidation peaks appeared at 2.48 V and 2.57 V, respectively, which reflected the formation of Li_2S_x ($1 < x < 4$) and a S_8 ring. In contrast, the air-CNT&S electrode possessed stronger polarization of the CV peaks compared with the CO_2-CNTs&S electrode. The sharper redox peak of the CO_2-CNTs&S electrode indicated a more kinetically efficient reaction process, which was mainly attributed to a shorter lithium ion diffusion distance. The smaller hysteresis of the corresponding redox peaks suggested slight polarization and robust electrochemical reversibility in the CO_2-CNTs&S electrode. These results indicated that the uniform deposition of sulfur/Li_2S on the CNTs prevented local charge accumulation, leading to alleviation of polarization.

The electrochemical properties of the air-CNT&S and CO_2-CNT&S composites were characterized by EIS (Fig. 5b). The apex

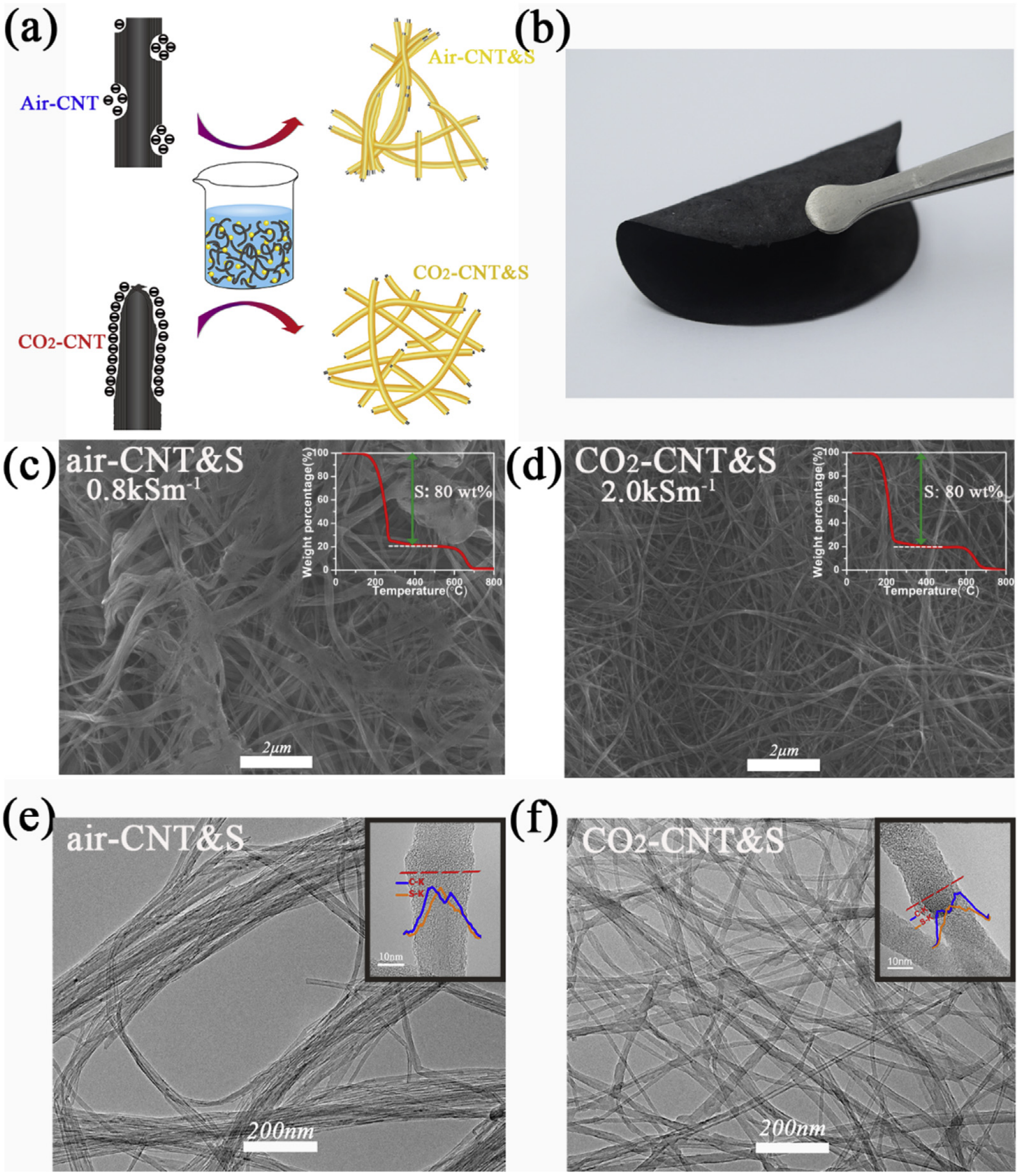

Fig. 4. (a) Schematic diagram of the synthesis procedure of the air-CNT&S and CO_2-CNT&S composites. (b) Photograph of a flexible and free-standing CO_2-CNT&S electrode. SEM images of (c) air-CNT&S and (d) CO_2-CNT&S composites. The insets of (c) and (d) show the TGA profiles of the CNT&S composites. TEM images of (e) air-CNT&S and (d) CO_2-CNT&S composites. The insets of (e) and (f) show the EDS line scan of carbon and sulfur on the segments of the air-CNT&S and CO_2-CNT&S, respectively. (A colour version of this figure can be viewed online.)

frequencies were 3.44 and 573.49 Hz for the air-CNT&S and CO_2-CNT&S electrodes, respectively. The ohmic resistance R_{ohm} (indicated by the intersection of the curve with the real axis at high frequency in inset of Fig. 5b) reflected the electronic resistance of the CNT&S composites, electrolyte, and separator. In this work, the electrolyte/separator was the same for the two electrodes. Therefore, the smaller R_{ohm} of the CO_2-CNTs&S cathode (4.7 Ω) compared with the air-CNT&S cathode (5.5 Ω) was in good agreement with the electrical conductivity measurements, and would be beneficial for sulfur utilization and cycling performance. The diameter of the semicircle in the high-frequency regions (Fig. 5b) demonstrated that the charge-transfer resistance (R_{ct}) of CO_2-CNT&S and air-CNT&S composites was 164 Ω and 1200 Ω, respectively. The smaller charge-transfer resistance of the CO_2-CNT&S composite was attributed to the more uniform structure and higher conductivity of the CO_2-CNT&S electrode. The sufficient active sites ensured rapid charge transport and faster reaction kinetics, which was beneficial for the better rate performance of the CO_2-CNT&S electrode.

Rate tests were performed on the CO_2-CNT&S and air-CNT&S electrodes with varied charge rates at a constant discharge rate of 0.2 C (Fig. 5c). The CO_2-CNT&S electrode delivered discharge capacities of 560.2, 529.1, 508.3, and 459.6 mA h g^{-1}_{sulfur} at 0.5 C, 1 C, 2 C, and 5 C charge rates, respectively. The air-CNT&S electrode exhibited inferior rate performances, and a significant capacity collapse was observed at 5 C. Charge/discharge curves of the air-CNT&S and CO_2-CNT&S electrodes at various charge rates are shown in Fig. S5. The voltage increase is denoted as IR-increase, when discharging is switched to charging. As the charge rate increased, the IR-raise of the air-CNT&S electrode increased much faster than that of the CO_2-CNT&S electrode (Table S2). The large IR-raises of the air-CNT&S electrode especially at high rates indicated the large contact resistance, serious local polarization, and slow

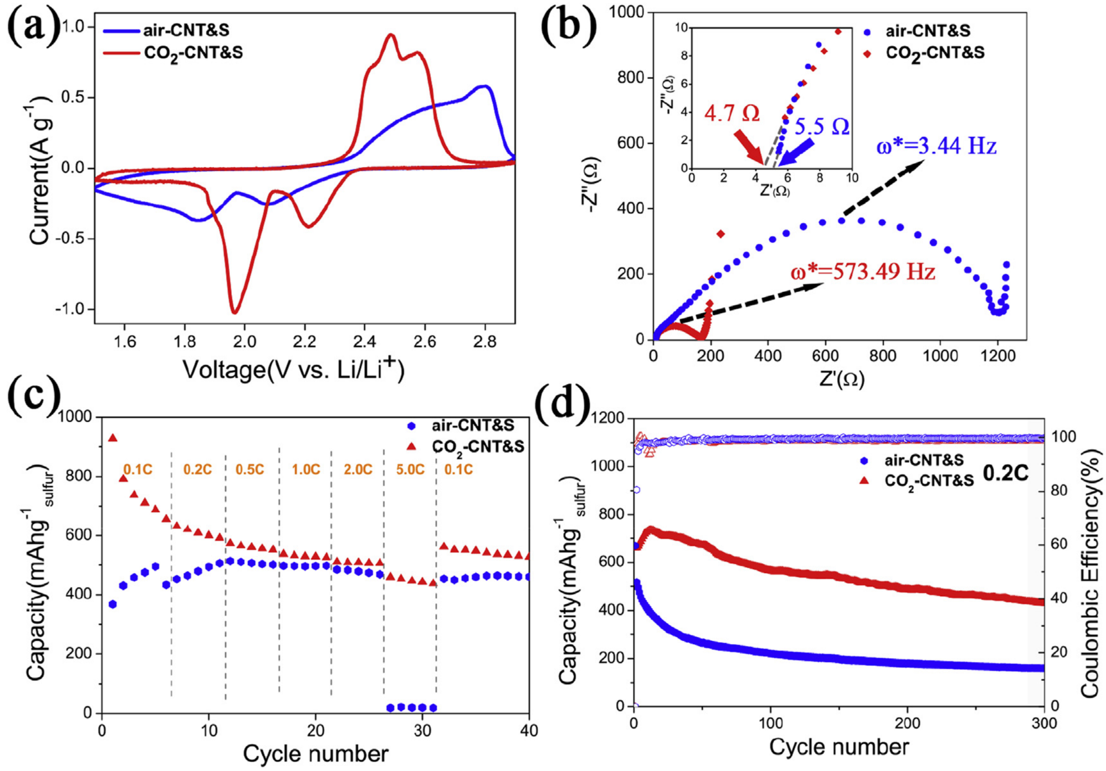

Fig. 5. (a) CV profiles, (b) EIS spectra, (c) rate performance, and (d) cycle performance at 0.2 C of the air-CNT&S and CO_2-CNT&S composites. (A colour version of this figure can be viewed online.)

reaction kinetics, which originated from the limited dispersion stability of the air-CNTs, aggregation of both air-CNTs and S/Li_2S particles, and insufficient charge transfer at the CNT/S interfaces. At relatively low charge rate (≤2C), the air-CNT&S electrode still demonstrated a capacity around 500 mA h $g^{-1}{}_{sulfur}$ and the initial charge potential was within the working voltage ranges. However, at high charge rate of 5C, the initial charge potential exceeded the cut-off voltage of the cell due to the large IR-raise, resulting in a sharp capacity decrease. On the contrary, the lower IR-raises at high rates in CO_2-CNT&S electrodes suggested lower contact resistance, less degree of polarization, and more efficient charge transfer, which as ascribed to the superior dispersion stability of the CO_2-CNTs, homogenous distribution of CO_2-CNT and S/Li_2S particles, and efficient charge transfer at CNT/S interfaces. Therefore, the CO_2-CNT&S electrode exhibited excellent rate performance.

The long-term cycling stability of the air-CNT&S and CO_2-CNT&S electrodes was also tested at a cycling rate of 0.2 C for 300 cycles (Fig. 5d). The specific capacity of the CO_2-CNT&S electrode increased gradually to 736.2 mA h $g^{-1}{}_{sulfur}$ after 12 cycles because the excess deep-buried sulfur needed a long activation process to become active [13]. The electrode maintained a capacity of 430.5 mA h $g^{-1}{}_{sulfur}$ after 300 cycles, corresponding to a small fade rate of 0.172% per cycle. In contrast, the air-CNT&S electrode exhibited a slightly lower initial capacity of 660.8 mA h $g^{-1}{}_{sulfur}$ and faded to 265.1 mA h $g^{-1}{}_{sulfur}$ after 50 cycles, which indicated a faster capacity degradation. After 300 cycles, only 159.4 mA h $g^{-1}{}_{sulfur}$ discharge capacity was available. Considering the sulfur loading, the areal capacities after 300 cycles were 0.60 and 0.22 mA h cm^{-2} for the CO_2-CNT&S and air-CNT&S electrodes, respectively. The CO_2-CNT&S electrode displayed superior cycling stability compared with that of the air-CNT&S electrode.

The performance of the CO_2-CNT&S electrode was compared with other oxidation treated CNT&S electrodes (including acid oxidation, pre-acid oxidation with KOH activation, water steam etching and air oxidation) reported in the literature in Table 1 [9,39,58,59]. The CO_2-CNT&S electrode demonstrated advantages of simple and solvent-free oxidation process, free-standing and flexible structure without using any binder/current collector, high sulfur content (80 wt%), excellent cycling stability (-0.17% decay per cycle for 300 cycles), and high rate performance (459.6 mA h g^{-1} at 5C). This work mainly compared the air-CNT&S and CO_2-CNT&S electrodes. As shown in our previous work, the air-CNT&S electrodes achieved excellent electrochemical performances with a lower sulfur content ranging from 50 to 70 wt% [39]. However, when the sulfur content was further raised to 80 wt%, the electrodes suffered from fast capacity decay and cycling instability owing to the poor dispersion of the air-CNTs and sulfur. In comparison, the CO_2-CNT&S electrode with a uniform distribution of sulfur displayed superior electrochemical performance at a sulfur content of 80 wt%. The electrochemical performance of sulfur electrodes is largely dependent on the dispersion properties of the CNTs in the composites. A well-dispersed CNT&S network provides a high conductivity of the electrode, a short lithium ion diffusion distance, and sufficient redox sites for high sulfur content, resulting in low polarization, little kinetic barriers during cycling, stable cycling performance, and excellent rate capability. The strategy presented in this work will open the door toward the development of high-performance Li–S batteries with high sulfur loading and might also be extended to other CNT-based energy storage systems.

4. Conclusion

A pre-oxidation treatment of CNTs by CO_2 is proposed to improve the electrochemical performance of CNT&S electrodes with high sulfur content. The oxidation process by CO_2 changed the hybridization of numerous carbon atoms from sp^2 to sp^3; the sp^3

Table 1
Electrochemical properties of various oxidation treated CNT&S electrodes in Li-S batteries.

CNT&S electrodes	S content (wt%)	Capacity decay (% per cycle)	High rate performance	References
Acid-oxidized CNT&S	65	−0.63%@0.2C(100th)	–	[58]
Pre-acid treatment +KOH activated CNT&S	80	−0.11%@0.2C(200th)	540.4 mA h g^{-1} (5C)	[59]
H_2O steam etched CNT&S	78–89	−0.19%@0.2C(200th)	150 mA h g^{-1} (15C)	[9]
Air-CNT&S	70	−0.31%@0.2C(100th)	655 mA h g^{-1} (5C)	[39]
CO_2-CNT&S	80	−0.17%@0.2C(300th)	459.6 mA h g^{-1} (5C)	This work

carbons with functional groups were confirmed to carry the negative charges on the external surface of the tubes. The negative charges introduced by CO_2 oxidation were revealed to be sufficient and uniformly distributed, which provided electrostatic repulsive forces to enable a stable efficient dispersal of CO_2-CNTs. The sulfur-loading capability of oxidized-CNTs was found to rely on the dispersion stability of the CNTs. The superior stable dispersion of the CO_2-CNTs provided more sulfur-loading sites and enhanced sulfur utilization compared with air-CNTs. A binder-free and uniformly dispersed CO_2-CNT&S electrode with a sulfur content of 80 wt% was fabricated through a sonication-assisted method. The CO_2-CNT&S electrode displayed advantages of such as better dispersion, higher conductivity, shorter lithium ion diffusion distance, low polarization, and faster charge transport at the interface of the electrode and electrolyte compared with the air-CNT&S electrode. Therefore, the CO_2-CNT&S electrode exhibited better cycling stability and superior rate performance than the air-CNT&S electrode. This work provides valid evidence of the advantages of the CO_2 oxidation treatment for the dispersion of CNTs and paves a way for high-sulfur-content CNT&S electrodes and other CNT composites.

Acknowledgements

This work was supported by NSFC (51472141), and the National Key Research and Development Program of China (2017YFA0205800).

Appendix A. Supplementary data

Supplementary data related to this article can be found at https://doi.org/10.1016/j.carbon.2018.02.048.

References

[1] X. Ji, K.T. Lee, L.F. Nazar, A highly ordered nanostructured carbon-sulphur cathode for lithium-sulphur batteries, Nat. Mater. 8 (6) (2009) 500–506.
[2] H. Yamin, et al., Lithium sulfur battery oxidation/reduction mechanisms of polysulfides in THF solutions, J. Electrochem. Soc. 135 (5) (1988) 1045–1048.
[3] J. Shim, K.A. Striebel, E.J. Cairns, The lithium/sulfur rechargeable cell effects of electrode composition and solvent on cell performance, J. Electrochem. Soc. 149 (10) (2002) A1321–A1325.
[4] Z. Li, et al., Insight into the electrode mechanism in lithium-sulfur batteries with ordered microporous carbon confined sulfur as the cathode, Adv. Energy Mater. 4 (7) (2014) 1301473.
[5] X. Yang, et al., Sulfur-infiltrated graphene-based layered porous carbon cathodes for high-performance lithium–sulfur batteries, ACS Nano 8 (5) (2014) 5208–5215.
[6] W. Ahn, et al., Sulfur nanogranular film-coated three-dimensional graphene sponge-based high power lithium sulfur battery, ACS Appl. Mater. Interfaces 8 (3) (2016) 1984–1991.
[7] T. Lin, et al., Scotch-tape-like exfoliation of graphite assisted with elemental sulfur and graphene–sulfur composites for high-performance lithium-sulfur batteries, Energy Environ. Sci. 6 (4) (2013) 1283.
[8] L. Sun, et al., Sulfur nanocrystals confined in carbon nanotube network as a binder-free electrode for high-performance lithium sulfur batteries, Nano Lett. 14 (7) (2014) 4044–4049.
[9] Z. Xiao, et al., Porous carbon nanotubes etched by water steam for high-rate large-capacity lithium–sulfur batteries, J. Mater. Chem. 2 (23) (2014) 8683.
[10] G. Zhou, Y. Zhao, A. Manthiram, Dual-Confined flexible sulfur cathodes encapsulated in nitrogen-doped double-shelled hollow carbon spheres and wrapped with graphene for Li–S batteries, Adv. Energy Mater. 5 (9) (2015).
[11] G. Zhou, et al., A graphene-pure-sulfur sandwich structure for ultrafast, long-life lithium-sulfur batteries, Adv Mater 26 (4) (2014) 625–631, 664.
[12] Q. Pang, et al., Review—the importance of chemical interactions between sulfur host materials and lithium polysulfides for advanced lithium-sulfur batteries, J. Electrochem. Soc. 162 (14) (2015) A2567–A2576.
[13] B. Papandrea, et al., Three-dimensional graphene framework with ultra-high sulfur content for a robust lithium–sulfur battery, Nano Research 9 (1) (2016) 240–248.
[14] A. Manthiram, S.H. Chung, C. Zu, Lithium-sulfur batteries: progress and prospects, Adv Mater 27 (12) (2015) 1980–2006.
[15] R. Yazami, Nanomaterials for Lithium-ion Batteries: Fundamentals and Applications, Pan Stanford Publishing, 2013.
[16] S. Rehman, et al., 3D vertically aligned and interconnected porous carbon nanosheets as sulfur immobilizers for high performance lithium-sulfur batteries, Adv. Energy Mater. 6 (12) (2016) 1502518.
[17] H. Chen, et al., Rational design of cathode structure for high rate performance lithium-sulfur batteries, Nano Lett. 15 (8) (2015) 5443–5448.
[18] R. Fang, et al., 3D interconnected electrode materials with ultrahigh areal sulfur loading for Li-S batteries, Adv Mater 28 (17) (2016) 3374–3382.
[19] Z. Yuan, et al., Hierarchical free-standing carbon-nanotube paper electrodes with ultrahigh sulfur-loading for lithium-sulfur batteries, Adv. Funct. Mater. 24 (39) (2014) 6105–6112.
[20] G. Zhou, et al., A flexible nanostructured sulphur–carbon nanotube cathode with high rate performance for Li-S batteries, Energy Environ. Sci. 5 (10) (2012) 8901.
[21] R. Fang, et al., Single-wall carbon nanotube network enabled ultrahigh sulfur-content electrodes for high-performance lithium-sulfur batteries, Nano Energy 42 (2017) 205–214.
[22] A. Hirsch, O. Vostrowsky, Functionalization of carbon nanotubes, in: Functional Molecular Nanostructures, Springer, 2005, pp. 193–237.
[23] J. Liu, et al., Fullerene pipes, Science 280 (5367) (1998) 1253–1256.
[24] M.A. Hamon, et al., Dissolution of single-walled carbon nanotubes, Adv. Mater. 11 (10) (1999) 834–840.
[25] J.S. Oh, K.H. Ahn, J.S. Hong, Dispersion of entangled carbon nanotube by melt extrusion, Korea Aust. Rheol. J. 22 (2) (2010) 89–94.
[26] H. Hu, et al., Influence of the zeta potential on the dispersability and purification of single-walled carbon nanotubes, J. Phys. Chem. B 109 (23) (2005) 11520–11524.
[27] B. Smith, et al., Colloidal properties of aqueous suspensions of acid-treated, multi-walled carbon nanotubes, Environ. Sci. Technol. 43 (3) (2009) 819–825.
[28] E. Heister, et al., Higher dispersion efficacy of functionalized carbon nanotubes in chemical and biological environments, ACS Nano 4 (5) (2010) 2615–2626.
[29] S.A. Ntim, et al., Size dependent aqueous dispersibility of carboxylated multiwall carbon nanotubes, J. Environ. Monit. 14 (10) (2012) 2772–2779.
[30] B. Koh, W. Cheng, Mechanisms of carbon nanotube aggregation and the reversion of carbon nanotube aggregates in aqueous medium, Langmuir 30 (36) (2014) 10899–10909.
[31] Q. Li, Anisotropic Nanomaterials, Springer, 2015.
[32] N.I. Kovtyukhova, et al., Individual single-walled nanotubes and hydrogels made by oxidative exfoliation of carbon nanotube ropes, J. Am. Chem. Soc. 125 (32) (2003) 9761–9769.
[33] M.S. Shaffer, X. Fan, A. Windle, Dispersion and packing of carbon nanotubes, Carbon 36 (11) (1998) 1603–1612.
[34] Y. Wu, et al., Applications of carbon nanotubes in high performance lithium ion batteries, Frontiers of Physics 9 (3) (2013) 351–369.
[35] S. Luo, et al., Binder-free LiCoO2/carbon nanotube cathodes for high-performance lithium ion batteries, Adv Mater 24 (17) (2012) 2294–2298.
[36] K. Jiang, Q. Li, S. Fan, Nanotechnology: spinning continuous carbon nanotube yarns, Nature 419 (6909) (2002), 801–801.
[37] L. Sun, et al., Super-aligned carbon nanotube/graphene hybrid materials as a framework for sulfur cathodes in high performance lithium sulfur batteries, J. Mater. Chem. A 3 (10) (2015) 5305–5312.
[38] W. Kong, et al., Binder-free polymer encapsulated sulfur–carbon nanotube composite cathodes for high performance lithium batteries, Carbon 96 (2016) 1053–1059.
[39] L. Sun, et al., Sulfur embedded in a mesoporous carbon nanotube network as a binder-free electrode for high-performance lithium-sulfur batteries, ACS Nano

10 (1) (2016) 1300–1308.
[40] K. Jiang, et al., Superaligned carbon nanotube arrays, films, and yarns: a road to applications, Adv. Mater. 23 (9) (2011) 1154–1161.
[41] S. Tsang, P. Harris, M. Green, Thinning and opening of carbon nanotubes by oxidation using carbon dioxide, Nature-London 362 (1993), 520–520.
[42] N. Yao, et al., Structure and oxidation patterns of carbon nanotubes, J. Mater. Res. 13 (09) (1998) 2432–2437.
[43] S. Yang, et al., Insights into the oxidation mechanism of sp2-sp3 hybrid carbon materials: preparation of a water-soluble 2D porous conductive network and detectable molecule separation, Langmuir 33 (4) (2017) 913–919.
[44] Y.-T. Kim, T. Mitani, Competitive effect of carbon nanotubes oxidation on aqueous EDLC performance: balancing hydrophilicity and conductivity, J. Power Sources 158 (2) (2006) 1517–1522.
[45] T. Lin, I.W. Chen, F. Liu, C. Yang, H. Bi, F. Xu, et al., Nitrogen-doped mesoporous carbon of extraordinary capacitance for electrochemical energy storage, Science 350 (6267) (2015) 1508–1513.
[46] S. Dag, et al., Oxygenation of carbon nanotubes: atomic structure, energetics, and electronic structure, Phys. Rev. B 67 (16) (2003).
[47] M.R. Smith, et al., Selective oxidation of single-walled carbon nanotubes using carbon dioxide, Carbon 41 (6) (2003) 1221–1230.
[48] F.M. Menger, M.E. Chlebowski, Is the ether group hydrophilic or hydrophobic? Langmuir 21 (7) (2005) 2689–2695.
[49] D. Bom, et al., Thermogravimetric analysis of the oxidation of multiwalled carbon nanotubes: evidence for the role of defect sites in carbon nanotube chemistry, Nano Lett. 2 (6) (2002) 615–619.
[50] Y.-C. Hsieh, Thermal Analysis of Multi-walled Carbon Nanotubes by Kissinger's Corrected Kinetic Equation, Aerosol and Air Quality Research, 2010.
[51] J. Gallego, C. Batiot-Dupeyat, F. Mondragón, Activation energies and structural changes in carbon nanotubes during different acid treatments, J. Therm. Anal. Calorim. 114 (2) (2013) 597–602.
[52] S.A. Chernyak, et al., Mechanism of thermal defunctionalization of oxidized carbon nanotubes, J. Phys. Chem. C 120 (31) (2016) 17465–17474.
[53] K. Behler, et al., Effect of thermal treatment on the structure of multi-walled carbon nanotubes, J. Nanoparticle Res. 8 (5) (2006) 615–625.
[54] A.A. Mamedov, et al., Molecular design of strong single-wall carbon nanotube/polyelectrolyte multilayer composites, Nat. Mater. 1 (3) (2002) 190–194.
[55] B.D. Levin, et al., Characterization of sulfur and nanostructured sulfur battery cathodes in electron microscopy without sublimation artifacts, Microsc. Microanal. 23 (1) (2017) 155–162.
[56] C. Raiß, et al., Pitfalls in the characterization of sulfur/carbon nanocomposite materials for lithium–sulfur batteries, Carbon 79 (2014) 245–255.
[57] S. Gong, Z.H. Zhu, S.A. Meguid, Carbon nanotube agglomeration effect on piezoresistivity of polymer nanocomposites, Polymer 55 (21) (2014) 5488–5499.
[58] W. Kong, et al., Ultrathin MnO_2/graphene oxide/carbon nanotube interlayer as efficient polysulfide-trapping shield for high-performance Li-S batteries, Adv. Funct. Mater. 27 (18) (2017) 1606663.
[59] Y.C. Jeong, et al., Partially unzipped carbon nanotubes for high-rate and stable lithium–sulfur batteries, J. Mater. Chem. A 4 (3) (2016) 819–826.